NATIONAL AERONAUTICS AND SPACE ADMINISTRATION

ANALYSIS OF SCATTEROMETRY DATA FROM PISGAH CRATER

CRES TECHNICAL REPORT 118-2

By

J. R. Lundien
Remote Sensing Laboratory
University of Kansas
Lawrence, Kansas

August 1967

Prepared by the University of Kansas Center for Research, Inc., Engineering Science Division, Lawrence, Kansas for the National Aeronautics and Space Administration (NASA) under NASA Contract No. NSR 17-004-003 and NAS 9-7175

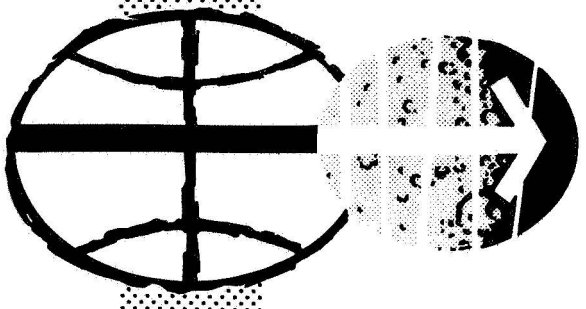

MANNED SPACECRAFT CENTER
HOUSTON, TEXAS

Technical Report
118-2

ANALYSIS OF SCATTEROMETRY DATA FROM PISGAH CRATER*

by

J. R. Lundien**

August 1967

The Remote Sensing Laboratory

* The research reported on here has been sponsored by the National Aeronautics and Space Administration under contract NSR 17-004-003 and NAS 9-7175. Reproduction in whole or in part is permitted for any purpose of the United States Government.

** At the time this report was written, Mr. Lundien was a student at the University of Kansas. He was on leave from the position of Supervisory Electrical Engineer at the U.S. Army Engineer Waterways Experiment Station in Vicksburg, Mississippi, under the "Civilian Training and Education Program of the Department of the Army."

ABSTRACT

The Ryan radar scatterometer was used to obtain data over the Pisgah Crater area in California. Nearly all the information in the σ_o versus θ curves was retained when the curves were represented by two straight line segments: one from 5 to 20 degrees and the other from 40 to 60 degrees. Areas of different geological type could be separated on the basis of slope-intercept values from the lines, though grouping patterns for each line were different. These grouping patterns may provide information on surface roughness.

Aircraft flight deviations produce errors in σ_o magnitude, errors in θ, and errors in the assumed position of the resolution cell. Factors are given to correct for the primary aircraft motions.

Analysis of Scatterometry Data From Pisgah Crater

Introduction

Radar return has been used to obtain information about the earth terrain for only the last few years. At first, radar images of poor photographic quality were all the analyst had to interpret, and although these images were made by systems not intended for terrain analysis, they produced results. This spurred the interest of many people to develop new systems and techniques for determining terrain properties with electromagnetic waves. Though built to obtain design data for lunar landing radars, the Ryan radar scatterometer has many features which make it attractive for remote sensing.[1]

The Ryan scatterometer can measure the radar backscattering cross section per unit surface area (σ_o) of various types of earth terrain for all angles of incidence (θ) out to $\pm$ 60 degrees from vertical. These measurements are made simultaneously by a single recording of the echo signal from the terrain and are separated into angular components using the doppler frequency in conjunction with knowledge of aircraft velocity and altitude.

This report presents the results of one flight (mission 21, fight 5) made with the Ryan scatterometer over the Pisgah Crater area in California on April 5, 1967. The data are correlated with 14 distinct geological areas along the flight path. In addition, correction factors have been derived which can be applied to the scatterometry data to correct for undesirable aircraft motion and for known earth profile changes.

System Operation

The Ryan scatterometry system uses a unique process for obtaining the σ_o versus θ curves. The equipment and methods are discussed in the following paragraphs.

A 1.5-watt klystron generates continuous-wave electromagnetic energy at a frequency of 13.3 GHz which is transmitted from the aircraft through an antenna with a Dolph-Chebishev design. An identical receiving antenna collects the energy reflected from the ground. The two-way antenna patterns have a very wide beamwidth of approximately 100 degrees along the flight path (see fig. 1) and a narrow 2.5 degree beamwidth across the flight path.* The antennas have low side lobe levels, are vertically polarized, and their patterns are centered on the vertical axis of the aircraft.

The energy collected from all angles by the receiving antenna is doppler coded by virtue of the aircraft motion and therefore contains the necessary information for θ separation. This received signal is detected by a direct-to-audio technique, amplified, and recorded on an FM tape recorder. The tapes are then available for processing at a later date.

Processing the tapes consists of playing the tapes back through a single sideband modulator to shift the doppler spectrum up to a carrier frequency or angle. The incidence angles for which the comb filters are set are $\pm$ 5, $\pm$ 10, $\pm$ 15, $\pm$ 20, $\pm$ 30, $\pm$ 40, $\pm$ 50, and $\pm$ 60 degrees. The bandwidth of each filter is set such that the resolution cell lengths along the flight path are identical and the 30 degree incidence angle resolution cell is square. The outputs from the filters are fed into an analog-to-digital converter and then into a digital computer. The computer program was written to give an output of σ_o versus θ for consecutive resolution cells along the flight path at the previously mentioned 8 incidence angles.

* After the data for this paper had been computer processed, it was found that σ_o at the aftbeam 60 degree incidence angle was in error. This was due to a corresponding error in fig. 1, the antenna gain pattern, and was caused by the shape of the aircraft upon which the antennas were mounted.

The computer program does not include σ_o corrections for undesirable aircraft motion or for measurable slope changes of the terrain along the flight path. This requires that flights be made under near perfect conditions for minimum σ_o error. The effect of some of this undesirable aircraft motion is discussed in the next section.

Scatterometry Measurement

Before becoming involved in the manipulation of data, a check should be made on the statistical fluctuation of individual measurements. In particular, the number of independent samples n_i occuring during the time for the radar to pass through a resolution length ℓ should be calculated. This is given by [2]

$$n_i = \frac{\text{TIME TO TRAVERSE } \ell}{\text{TIME/SAMPLE}}$$

$$\cong \frac{\ell/V}{1/4\Delta fs} = \frac{4\ell\Delta fs}{V}$$

where V is the aircraft velocity and Δf_s is the width of the processing filter. Using the data from this flight, n_i was found to vary from 1090 at 5 degrees to 138 at 60 degrees. This does provide an adequate limit for the statistical fluctuations.

It was assumed on all the scatterometry flights that only minor deviations were present in the aircraft flight path and in the slope of the terrain under investigation. This assumption enabled the analyst to use a constant range value for each angle of incidence in calculating σ_o. However, there are a number of undesirable aircraft motions which can affect the accuracy of the σ_o versus θ measurements. Correction factors can be found and applied to the data for each motion type or, if not applied, can give the analyst some idea of the data accuracy and explain some of the random fluctuations in the data.

There are three ways in which aircraft flight deviations produce errors. They are: a) error in σ_o magnitude, b) error in θ, and c) error in the assumed position of the resolution cell. The error in σ_o magnitude due to range errors is small enough to be neglected under normal operating conditions (see table 1). Of the three error types, the error in the assumed position of the resolution cell may be the most serious when only small homogeneous areas are present on the terrain under investigation. It could be possible to miss small geological areas entirely or to locate their responses in the wrong place.

The error in θ can affect data accuracy at all incidence angles. The slope in the σ_o versus θ curve may get as high as 2 or 3 db per degree at

the 5 degree incidence angle for certain types of terrain. [3] Thus, for example, only a small error of 3 degrees in θ could produce 6 to 9 db error in σ_o. The slope in the σ_o versus θ curve falls off when θ increases past 5 or 10 degrees. However, the antenna pattern is angle sensitive and becomes most severe for a 60 degree angle, though still present in varying amounts for angles between 10 and 50 degrees (see fig. 1). The two-way antenna gain pattern has dips and peaks over its 100 degree beamwidth. The slopes lie in the neighborhood of $\pm$ 0.5 to 1.0 db per degree and for angles greater than 50 degrees the slope is approximately -1.0 db per degree. An error of 5 degrees in θ, for example, would give a 5 db error in σ_o at the large incidence angles.

Unfortunately, much of the same sensitivity is produced by the slope of the terrain as well as by the aircraft motion discussed in the following paragraphs. Example calculcations are given in Table I for all the error types.

Vertical Change

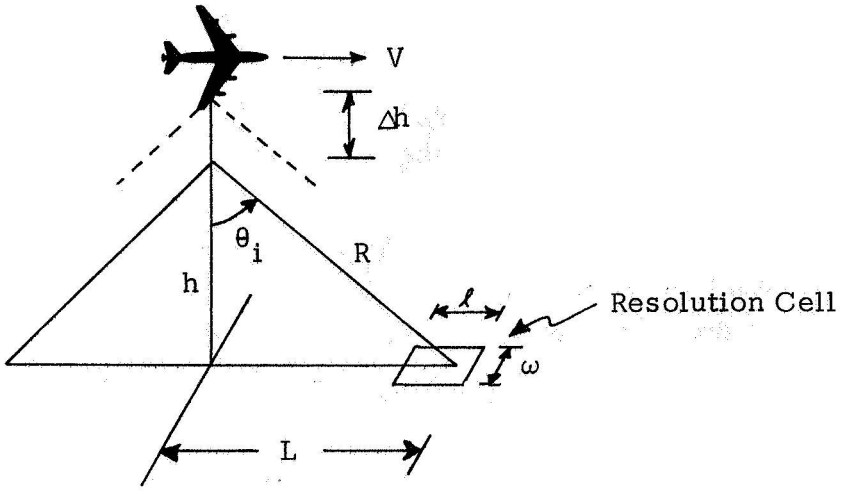

For the figure above, let;

V = Velocity

h = Height of antennas above terrain

Δh = Change in height

R = Slant range from antennas to resolution cell center

ω = Resolution cell width

ℓ = Resolution cell length

L = Horizontal distance to center of resolution cell

θ_i = Incidence angle

ϕ = Angular width of the resolution cell

$\Delta\theta_i$ = Angular length of the resolution cell at some θ_i

a) σ_o correction factor:

The range (R) and resolution cell length (ℓ) and width (ω) under normal operation conditions are given below:

$$R = h/\cos\theta_i$$
$$\omega = 2R\,\text{TAN}\,\phi/2 = 2(h/\cos\theta_i)\,\text{TAN}\,\phi/2$$
$$\ell = h[\text{TAN}(\theta_i + \Delta\theta_i/2) - \text{TAN}(\theta_i - \Delta\theta_i/2)]$$

The range and resolution cell length and width after a change in height of Δh are:

$$R_{\Delta h} = (h+\Delta h)/\cos\theta_i$$
$$\omega_{\Delta h} = 2(h+\Delta h)(1/\cos\theta_i)\,\text{TAN}\,\phi/2$$
$$\ell_{\Delta h} = 2(h+\Delta h)[\text{TAN}(\theta_i + \Delta\theta_i/2) - \text{TAN}(\theta_i - \Delta\theta_i/2)]$$

The radar equation is:

$$\sigma_o = \frac{P_r (4\pi)^3 R^4}{P_t G_i^2 \lambda^2 A_i}$$

Where: P_r = Received signal power

P_t = Transmitted signal power

G_i = Gain of antenna in direction of θ_i

λ = Wavelength of transmitted signal

A_i = Area illuminated

$\cong \omega\ell$, assuming constant gain over the resolution cell area

Thus, the correction factor for σ_o becomes:

$$\frac{(\sigma_o)_{\Delta h}}{\sigma_o} = \frac{(R^4/\omega\ell)_{\Delta h}}{R^4/\omega\ell} = \left(\frac{h+\Delta h}{h}\right)^2$$

b) Resolution cell location:

Under normal conditions the distance from the center of the resolution cell to the point directly below the aircraft is given by:

$$L = h \text{ TAN } \theta_i$$

with a height change of Δh this distance becomes:

$$L_{\Delta h} = (h + \Delta h) \text{ TAN } \theta_i$$

or the resolution cell has moved ΔL to a new location where:

$$\Delta L = L_{\Delta h} - L = \Delta h \text{ TAN } \theta_i$$

Lateral Movement

a) There is no correction factor needed for σ_o for lateral movement of the aircraft.

b) The resolution cell moves by the same amount of the lateral movement.

Pitch

a) The error in σ_o due to pitch is produced in the same manner as that for an error in θ_i. The doppler frequency coding insures the proper incidence angle on flat terrain regardless of the pitch angle. The antennas are fixed on the sides of the aircraft so that pitch would tend to rotate the antenna beam through the resolution cell. The error in σ_o is approximately $\pm$ 0.5 to 1.0 db per degree of pitch for incidence angles between 10 to 50 degrees and -1.0 db per degree for the 60 degree angle of incidence. Also, the changes in σ_o will be opposite for the same angle in the fore and aft beams thus magnifying the difference in the two beams.

b) As mentioned above, the doppler coding insures no movement of the resolution cell with changes in pitch angles.

Crab

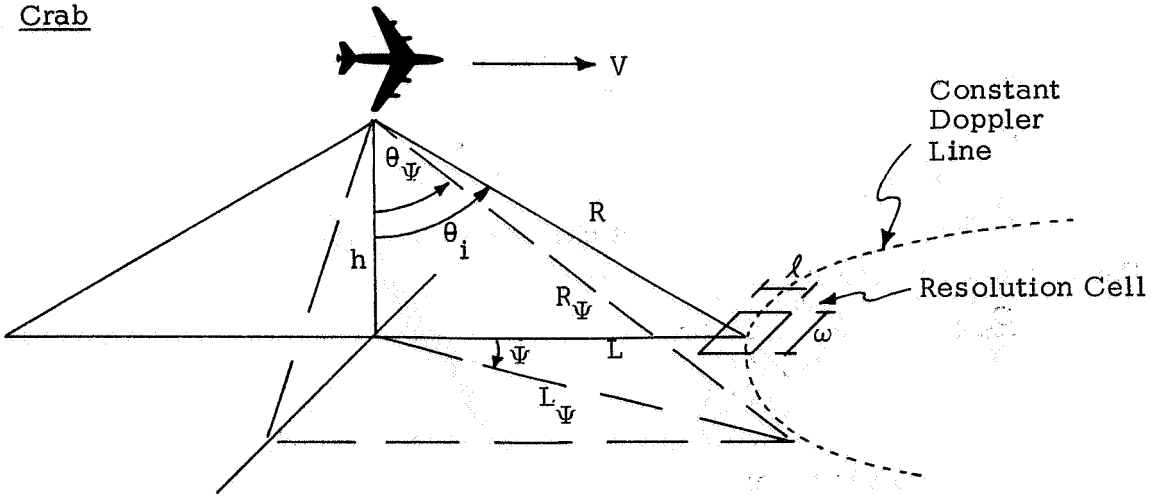

Under normal operating conditions when there is no crab ($\Psi = 0$), the doppler frequency f can be expressed by:

$$f = \frac{2V}{\lambda} \sin\theta_i$$

When crab is present in the aircraft flight, the expression for doppler frequency must be modified to account for the hyperbolic shape of the constant doppler lines fore and aft of the aircraft. Crab results in the beam reaching out a little farther and the incidence angle is increased. When $\Psi \neq 0$,

$$f = \frac{2V}{\lambda} \frac{L_\psi \cos\Psi}{R_\psi}$$

Since the resolution cell travels on a constant doppler line, the two expressions for doppler frequency must be equal.

$$f = \frac{2V}{\lambda} \sin\theta_i = \frac{2V}{\lambda} \frac{L_\psi \cos\Psi}{R_\psi}$$

or

$$\frac{L_\psi}{R_\psi} = \sin\theta_\psi = \frac{\sin\theta_i}{\cos\Psi}$$

and the new incidence angle is:

$$\theta_\psi = \sin^{-1}\left[\frac{\sin\theta_i}{\cos\Psi}\right]$$

The results of such an incidence angle change has been discussed previously.

a) σ_o correction factor

The range (R_Ψ) and resolution cell length (ℓ_Ψ) and width (ω_Ψ) when $\Psi \neq 0$ are:

$$R_\psi = h\left[\frac{\cos^2\Psi}{\cos^2\Psi - \sin^2\theta_i}\right]^{1/2}$$

$$\omega_\psi = 2R_\psi \tan\phi/2 = 2h\left[\frac{\cos^2\Psi}{\cos^2\Psi - \sin^2\theta_i}\right]^{1/2} \tan\phi/2$$

$$\ell_\psi = h\left[\tan(\theta_\psi + \Delta\theta_i/2) - \tan(\theta_\psi - \Delta\theta_i/2)\right]$$

$$= \frac{h \sin \Delta\theta_i}{\cos^2\theta_\psi - \sin^2 \Delta\theta_i/2}$$

and the correction factor for σ_o becomes

$$\frac{(\sigma_o)_\psi}{\sigma_o} = \left[\frac{\cos^2\psi \cos^2\theta_i}{\cos^2\psi - \sin^2\theta_i}\right]^{3/2} \left[\frac{\cos^2\theta_\psi - \sin^2 \Delta\theta_i/2}{\cos^2\theta_i - \sin^2 \Delta\theta_i/2}\right]$$

b) Resolution cell location:

The location of the resolution cell with aircraft crab is:

$$L_\psi = R_\psi \sin\theta_\psi$$

$$= \frac{h \sin\theta_i}{(\cos^2\psi - \sin^2\theta_i)^{1/2}}$$

which is

$$X = L_\psi \sin\psi = \frac{h \sin\theta_i \sin\psi}{(\cos^2\psi - \sin\theta_i)^{1/2}}$$

away from the flight line. The along-track displacement is

$$\Delta L = \frac{h \sin\theta_i \cos\psi}{(\cos^2\psi - \sin^2\theta_i)^{1/2}} - h\tan\theta_i$$

Roll

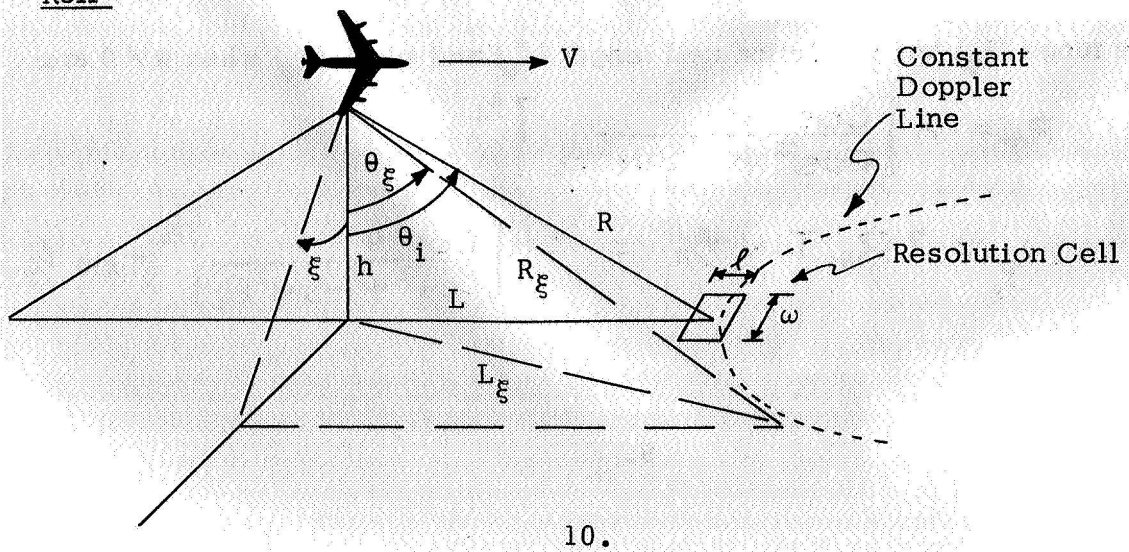

As with crab, roll causes the incidence angle to change. The expressions for the doppler frequency with and without roll are:

$$f = \frac{2V}{\lambda} \sin \theta_i$$

$$f = \frac{2V}{\lambda} \sin \left[\cos^{-1} \left(\frac{h/\cos \xi}{R_\xi} \right) \right]$$

Equating the two expressions under constant doppler frequency conditions give:

$$f = \frac{2V}{\lambda} \sin\theta_i = \frac{2V}{\lambda} \sin \left[\cos^{-1} \left(\frac{h/\cos \xi}{R_\xi} \right) \right]$$

or

$$\cos \theta_i = \frac{h/\cos \xi}{R_\xi} = \frac{\cos \theta_\xi}{\cos \xi}$$

and finally, the new incidence angle θ_ξ is:

$$\theta_\xi = \cos^{-1} [\cos \theta_i \cos \xi]$$

a) σ_o correction factor

The range (R_ξ) and resolution cell length (ℓ_ξ) and width (ω_ξ) when $\xi \neq 0$ are:

$$R_\xi = \frac{h}{\cos \xi \cos \theta_i}$$

$$\omega_\xi = \frac{2 R_\xi \tan \phi/2}{\cos \xi} = \frac{2h \tan \phi/2}{\cos^2 \xi \cos \theta_i}$$

$$\ell_\xi = h [\tan(\theta_\xi + \Delta\theta_i/2) - \tan (\theta_\xi - \Delta\theta_i/2)]$$

$$= \frac{h \sin \Delta\theta_i}{\cos^2 \theta_\xi - \sin^2 \Delta\theta_i/2}$$

and the correction factor for σ_o becomes:

$$\frac{(\sigma_o)_\xi}{\sigma_o} = \left(\frac{1}{\cos^2 \xi} \right) \left[\frac{\cos^2 \theta_\xi - \sin^2 \Delta\theta_i/2}{\cos^2 \theta_i - \sin^2 \Delta\theta_i/2} \right]$$

Note that the resolution cell is no longer square and since the product of the cell length and width is not the true cell area, the σ_o correction factor is only approximate.

b) Resolution cell location

The location of the resolution cell with aircraft roll is:

$$L_\xi = R_\xi \sin\theta_\xi = \frac{h\,(1-\cos^2\theta_i \cos^2\xi)^{1/2}}{\cos\xi\cos\theta_i}$$

which is:

$$X = h \tan\xi$$

away from the flight line. The along-track displacement is

$$\Delta L = h \tan\theta_i \left[\frac{1}{\cos\xi} - 1\right]$$

Location of errors on data

The data is presented as σ_o versus θ curves for each resolution cell. As described earlier, the σ_o values are measured at different times as the aircraft flies along to produce the different incidence angles. Thus, a malfunction of the equipment (i.e., power failure, recording dropout, etc.) or aircraft motion error will affect the σ_o values at all fore and aft incidence angles at one particular time. The results of such errors will appear as a false signal on a number of σ_o versus θ curves at different angles. In order to look for such false signals, the resolution cell shift with θ must be known. The horizontal distance from the aircraft to the resolution cell has been given as:

$$L = h \tan\theta_i$$

or

$$n = \frac{h}{d} \tan\theta_i$$ = number of resolution cells to sampling point

For the Pisgah Crater data, the values for the aircraft height and distance (d) between centers of adjacent resolution cells were 4,000 feet and 216 feet respectively. The following table can be completed:

θ_g	L, feet	n, cells
5^o	348	1.6
10^o	705	3.26
15^o	1072	4.96
20^o	1456	6.8
30^o	2310	10.7
40^o	3358	15.52
50^o	4760	22.04
60^o	6930	32.06

To determine the results of a malfunction or aircraft motion error, a search must be made for each θ at the indicated cell (n) fore and aft of the error point.

DATA ANALYSIS

Pisgah Crater has been of interest to remote sensing specialists for a number of years due to its varied geologic formations and lack of vegetation. This area has been a preferred testing site for NASA because it may possibly simulate conditions found on the lunar surface. For these reasons, a flight identified as Mission 21, Flight 5, Line 1, Run 3, was made with the Ryan scatterometer over Pisgah Crater.

Pisgah Crater was divided into 14 areas along the flight path by geologic composition (see fig. 2). These are listed in Table II. The scatterometry data obtained at 8 incidence angles from this flight are shown as forebeam data, figs. 3 and 4, and aftbeam data, figs. 5 and 6. The geologic areas in figs. 3-6 are indicated by number which correspond to those in Table I and the identification number references the data to the original σ_o versus θ curves (see fig. 7 for typical curve pair). Each identification number refers to data taken over a two resolution cell length.

The data were reduced by assuming that the σ_o versus θ curves could be formed in straight line segments similar to that of fig. 7; one from 5 to 20 degrees, another from 40 to 60 degrees, with the 30 degree σ_o value nearly the same as that of the 40 degree σ_o. Slope and intercept values were obtained for each of the straight line segments; a zero degree intercept value was used for the 5 to 20 degree line and a 50 degree intercept value used for the 40 to 60 degree line. The results of these measurements are shown in figs. 8-11 for the forebeam and aftbeam.

Results

The reflectance of electromagnetic energy from terrain is primarily quasi-specular at vertical incidence (near zero degrees) and represents the effects of both the electrical properties of the material and the surface roughness. At the large incidence angles, the reflectance from terrain is diffuse and is determined primarily by surface roughness.[4] However, the surface roughness affecting measurements at large and small incidence angles may not be of the same magnitude and type. A quasi-specular reflectance region will give a larger σ_o near vertical incidence and a smaller σ_o at large incidence angles than corresponding measurements made over a diffuse reflectance region.

The cross-over region between vertical type reflection and non-vertical type reflection is readily determined from the data as the angle for which σ_o is insensitive to changes in the type of terrain. This cross-over region can be interpreted as the break point between quasi-specular and diffuse reflectance. From the forebeam data (figs. 3 and 4) this cross-over region is approximately 13 degrees and does not seem to change much during the entire run. The cross-over region between vertical type and non-vertical type reflection for the aft-beam data is approximately 11 degrees and again is relatively constant over the entire run. The difference in the forebeam and aftbeam cross-over region suggests either an equipment misalignment, the antennas for example, or a natural geologic alignment. Such an alignment might be caused by erosion from rain or prevailing winds, or by the lava flow itself. If it can be found that the difference does not have a geologic origin, the cross-over region may have use as a calibration or reference point. Even if there is a geologic origin for the forebeam-aftbeam cross-over region difference, it may still be used to check for gross errors if it can be shown to vary 2 degrees or less over all terrain as indicated from this test.

The results of plotting slope versus the zero degree intercept for the 5 to 20 degree forebeam line is shown in figs. 12 and 13. It can be seen from fig. 12 that certain areas can be separated by merely using information from the first 20 degrees of the σ_o versus θ curves. The slope-intercept values clearly separate playa lake sediment (area 14) and alluvial material (areas 1 and 3) from the basalt flows and cinder cone area. Areas 1, 3, and 14 have been further divided into smaller pieces to show that even though an area is of one geologic type, it may not be uniform throughout in its σ_o measurements. Fig. 13 shows in more detail the porphyritic olivine basalt flows and suggests that the material in these areas, though separable to some extent, have similar surface roughness and electrical properties.

The 40 to 60 degree slope values are plotted versus the 50 degree intercept values in fig. 14. As seen in this fig., there appears to be far more contrast in the geological areas defined by the large incidence angle σ_o measurements than by the small incidence angle σ_o measurements of figs. 12 and 13. Of particular interest is the manner in which the 40 to 60 degree slope-intercept plot shows consecutive geologic areas blended into each other in order of appearance across the flight line. The overlap of areas shows that there are transitions between adjacent areas instead of an abrupt dividing line.

Fig. 15 shows the large and small scale roughness ranking of the 14 geological areas. This fig. was prepared from estimates made by people familiar with the Pisgah Crater area terrain and is not as precise as that which could be obtained from a rigorous roughness study. However, the roughness ranking shown in fig. 15 has definite similarities with the slop-intercept patterns in figs. 12-14 obtained from the scatterometry system. In particular, note the similarity in the large scale roughness ranking of fig. 15 with the 50 degree intercept ranking of fig. 14.

There are some spots in the data that appear to be in error and suggest other problems. Because of the lack of supporting evidence, these spots are merely listed below with a short discussion of the suspected problem. The comments are included in this paper to suggest improvements which can be made in the data gathering process and as a guide to future processing of scatterometer data.

a) Reference identification numbers 120-130 in aftbeam data and 105-120 in forebeam data of figs. 3-9. There is an abrupt change in the data that does not occur at the same place for the different incidence angles. This suggests that the resolution cell location changes with angle.

b) The terrain tends to slope away from the cinder cone, area 5. However, not all the differences in the forebeam and aftbeam data can be correlated with this slope. For example, compare the forebeam and aftbeam σ_o for area 12. If the area is homogeneous, it should have the same σ_o values in both directions with only statistical fluctuations appearing as differences between the two beams. This was also pointed out earlier in connection with the cross-over region between vertical type and non-vertical type reflection, and it was suggested that the difference may be caused by the scatterometer system itself. If, on the other hand, the area is not homogeneous, its σ_o values may be different in both directions because of roughness patterns.

c) Reference identification numbers 120-135 of forebeam σ_o curves, figs. 3 and 4. There is a peak in the σ_o values starting at identification number 121 at the 5 degree incidence angle, appears slightly later for consecutive θ curves, and ends at identification

number 133 at the 50 degree incidence angle. This shift with incidence angle has the same order and magnitude as described in the section titled, "Location of errors on data". This may be a false signal recorded in the aircraft at the time the Pisgah Crater flight was made.

CONCLUSIONS

The following conclusions are based on the calculations and test data in this paper.

a) The error in σ_o magnitude due to range errors produced by aircraft flight deviations is small enough to be neglected under normal operating conditions.

b) The error in θ and the error in assumed position of the resolution cell produced by aircraft flight deviations can become serious under certain conditions and should be investigated for each flight.

c) The cross-over region between vertical type and non-vertical type reflection is approximately 13 degrees for the forebeam and 11 degrees for the aftbeam. This cross-over region may prove useful as a calibration or reference angle.

d) Nearly all the σ_o versus θ curves could be represented by two straight lines to reduce the bulk of the data.

e) The slope-intercept values extracted from the linearized σ_o versus θ curves show similar grouping patterns to those from surface roughness and can be used to differentiate areas of different geologic type.

The results of the scatterometer measurements over Pisgah Crater indicate a high degree of success in separating areas of differing geologic type. It is doubtful that any remote sensing system can be found which will correctly identify soil or rock types 100 percent of the time. However, it may be possible to narrow the field down to a "group identity" by the process of elimination. It is only when more and more tests are made and analyzed that the similar can be set apart from the genuine.

REFERENCES

1. Floyd, W. L. "R F Reflectivity Measurements, Final Report", Ryan Aeronautical Company. Report No. 29174-9, April 1966.

2. Moore, R. K. "Radar Scatterometry -- An Active Remote Sensing Tool", CRES Report No. 61-11, University of Kansas, Lawrence, Kansas.

3. Lundien, J. R. "Terrain Analysis by Electromagnetic Means; Radar Responses to Laboratory Prepared Soil Samples Report" U.S. Army Engineer Waterways Experiment Station, C.E., Technical Report No. 3-693.

4. Rouse, J. W. Jr., W. P. Waite, and R. L. Walters "Use of Orbital Radars for Geoscience Investigations", CRES Report No. 61-8.

TABLE I

EXAMPLE CALCULATIONS FROM DERIVED EQUATIONS
(4000 ft. altitude)

	$\theta_i = 5^\circ$			$\theta_i = 30^\circ$			$\theta_i = 60^\circ$		
Vertical Change:									
Δh, feet	100	200	500	100	200	500	100	200	500
$(\sigma_o)_{\Delta h}/\sigma_o$, db	0.21	0.42	1.02	0.21	0.42	1.02	0.21	0.42	1.02
ΔL, feet	8.7	17.4	43.6	57.7	115.4	288.5	173.1	346.2	865.5
Crab:									
Ψ, degrees	5	10	15	5	10	15	5	10	15
θ_Ψ, degrees	5.0	5.1	5.2	30.1	30.5	31.2	60.3	61.6	63.8
$(\sigma_o)_\Psi/\sigma_o$, db	0	0	0	0.01	0.02	0.04	0.07	0.20	0.49
L_Ψ, feet	351	355	363	2322	2358	2420	7040	7392	8100
X, feet	31	62	94	202	409	626	614	1282	2096
ΔL, feet	2	2	3	8	12	30	80	350	890
Roll:									
ξ, degrees	5	10	15	5	10	15	5	10	15
θ_ξ, degrees	7.1	11.2	15.8	30.5	31.5	33.2	60.1	60.5	61.1
$(\sigma_o)_\xi/\sigma_o$, db	0	0	0	0	0	0	0	0	0
L_ξ, feet	496	791	1131	2356	2450	2620	6970	7070	7250
X, feet	348	705	1072	348	705	1072	348	705	1072
ΔL, feet	1	5	12	9	36	82	26	107	245

TABLE II GEOLOGIC NAMES OF AREAS

Area 1	Alluvial material
Area 2	Porphyritic olivine basalt flows of second eruptive phase plus windblown alluvial material
Area 3	Alluvial material
Area 4	Microporphyritic olivine basalt flows of first eruptive phase
Area 5	Cinder cone
Area 6	Porphyritic olivine basalt flows of final eruptive phase
Area 7	Porphyritic olivine basalt flows of second eruptive phase
Area 8	Porphyritic olivine basalt flows of secondary eruptive phase, faulted area
Area 9	Porphyritic olivine basalt flows of second eruptive phase
Area 10	Porphyritic olivine basalt flows of final eruptive phase
Area 11	Porphyritic olivine basalt flows of second eruptive phase
Area 12	Microporphyritic olivine basalt flows of first eruptive phase
Area 13	Lake sediments and basalt
Area 14	Playa Lake sediment

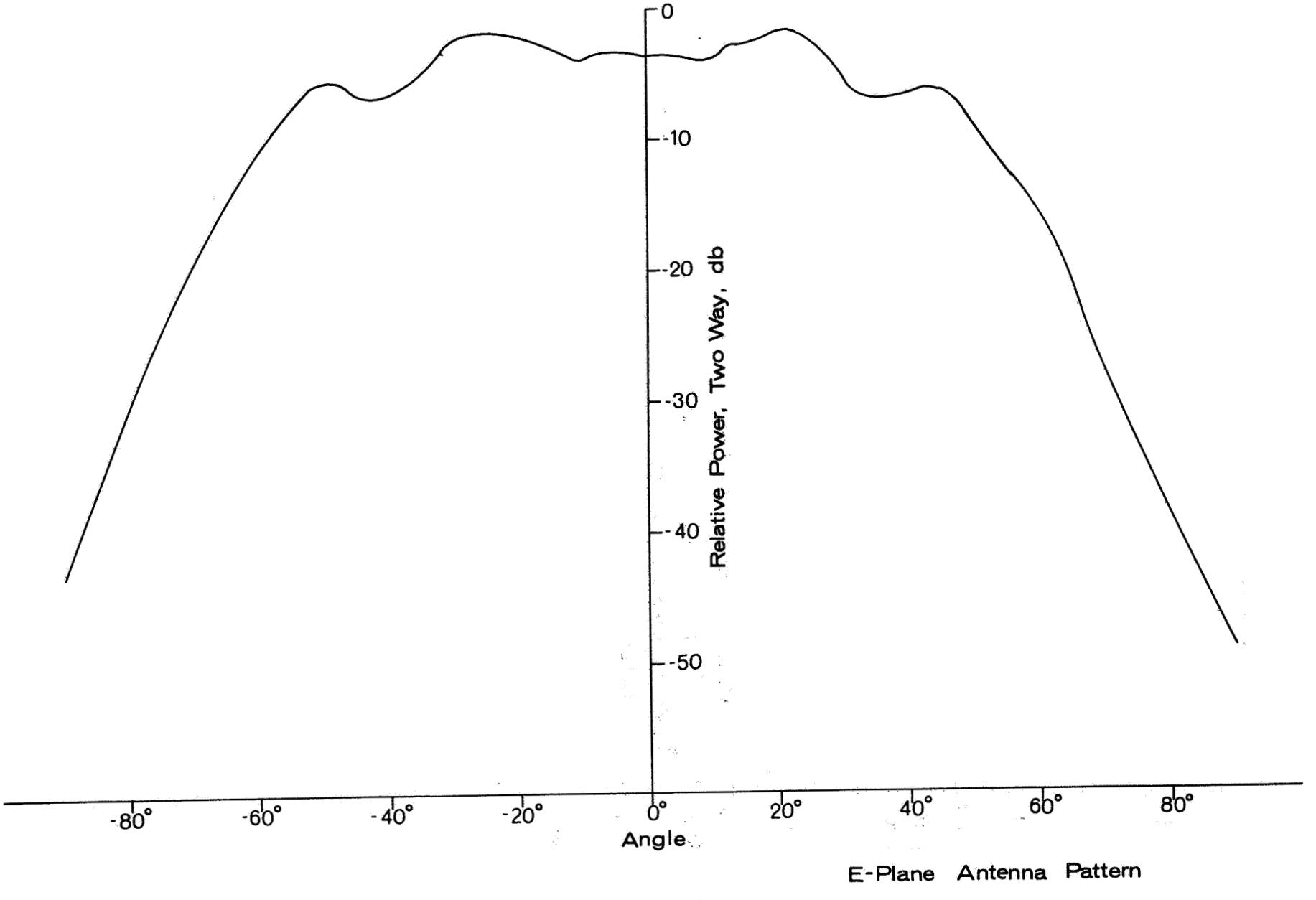
0
-10
-20
-30
-40
-50
Relative Power, Two Way, db
-80°
-60°
-40°
-20°
0°
20°
40°
60°
80°
Angle
E-Plane Antenna Pattern

Figure 1.

PISGAH CRATER

Area 1: Alluvial material

Area 2: Porphyritic olivine basalt flows of second eruptive phase plus windblown alluvial material

Area 3: Alluvial material

Area 4: Microporphyritic olivine basalt flows of first eruptive phase

Area 5: Cinder cone

Area 6: Porphyritic olivine basalt flows of final eruptive phase

Area 7: Porphyritic olivine basalt flows of second eruptive phase

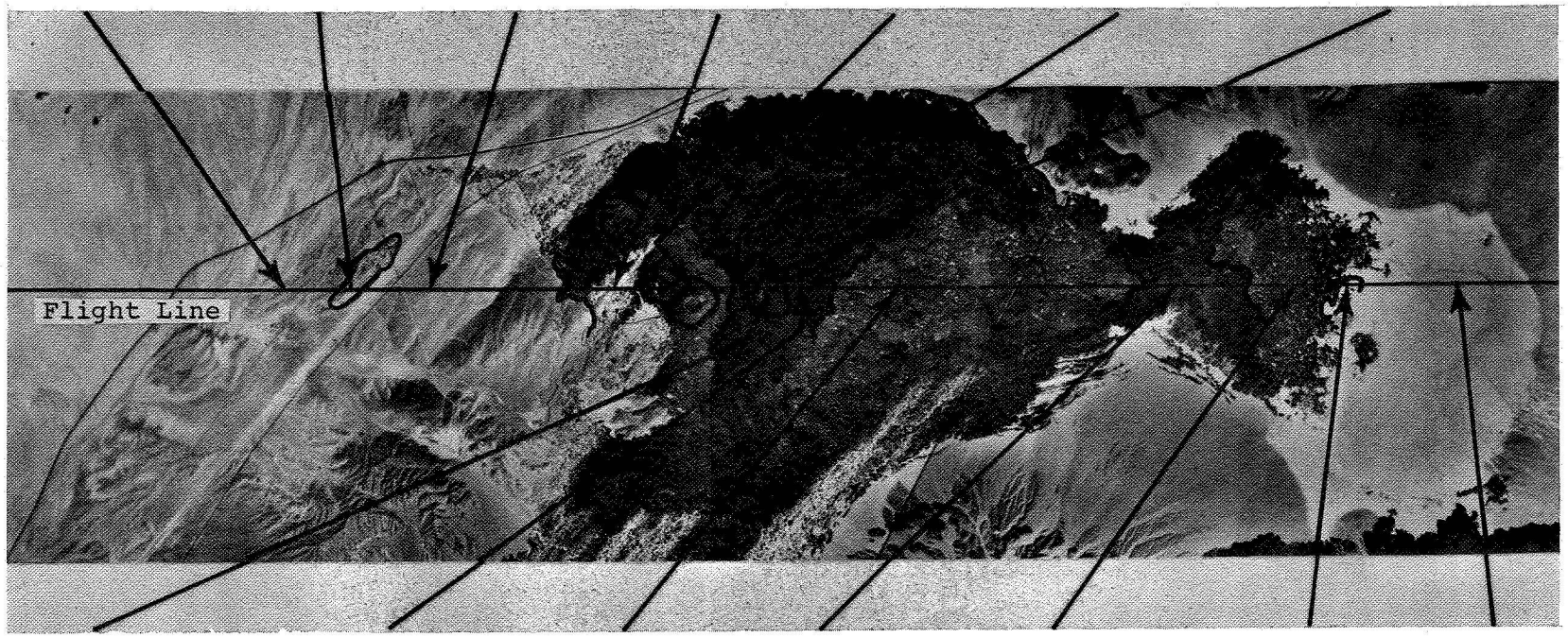

Area 8: Porphyritic olivine basalt flows of secondary eruptive phase faulted area

Area 9: Porphyritic olivine basalt flows of second eruptive phase

Area 10: Porphyritic olivine basalt flows of second eruptive phase

Area 11: Porphyritic olivine basalt flows of second eruptive phase

Area 12: Microporphritic olivine basalt flows of first eruptive phase

Area 13: Lake sediment and basalt

Area 14: Playa Lake sediment

Figure 2.

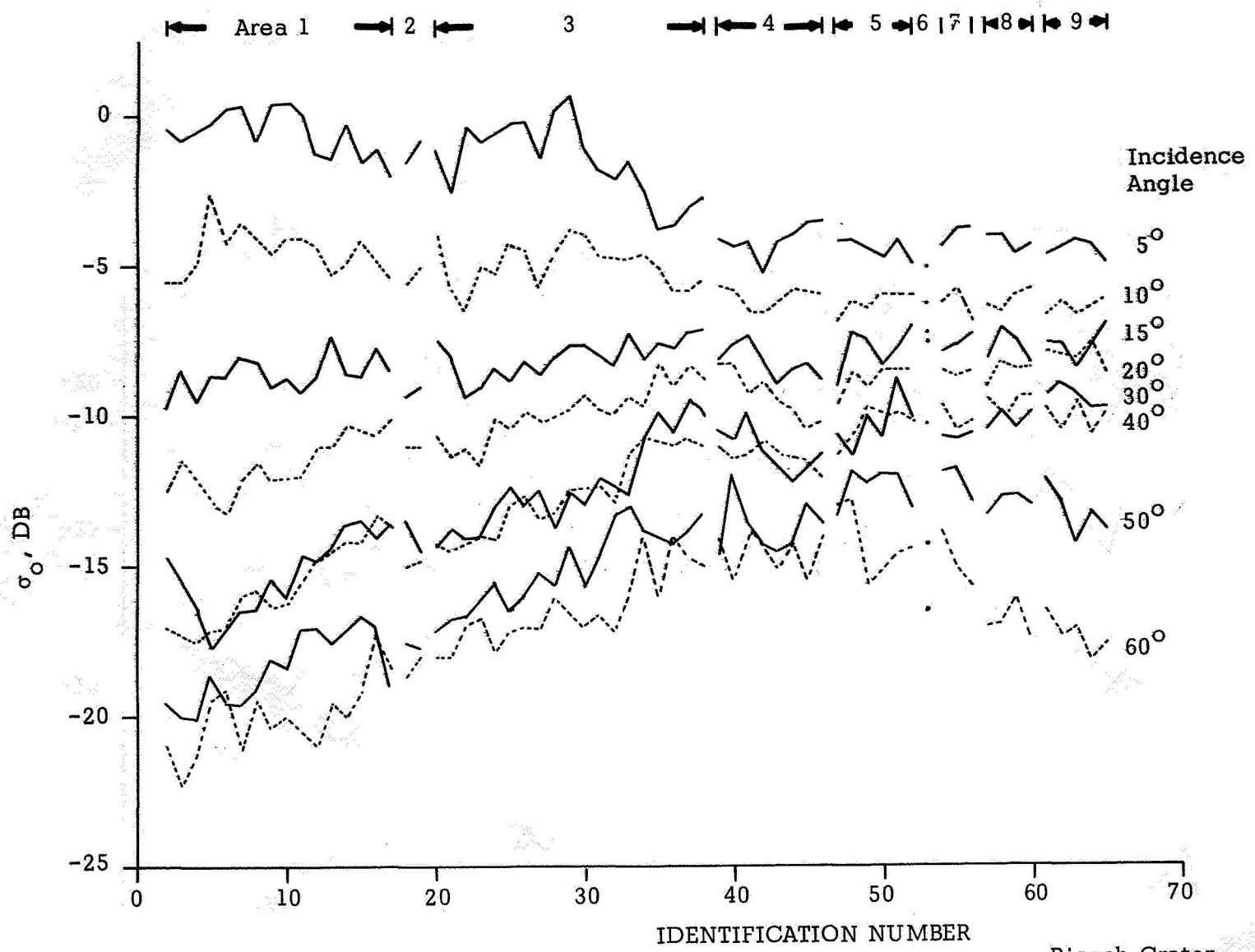

Pisgah Crater σ_o values

Forebeam, M 21-F5-L1-$3

Figure 3.

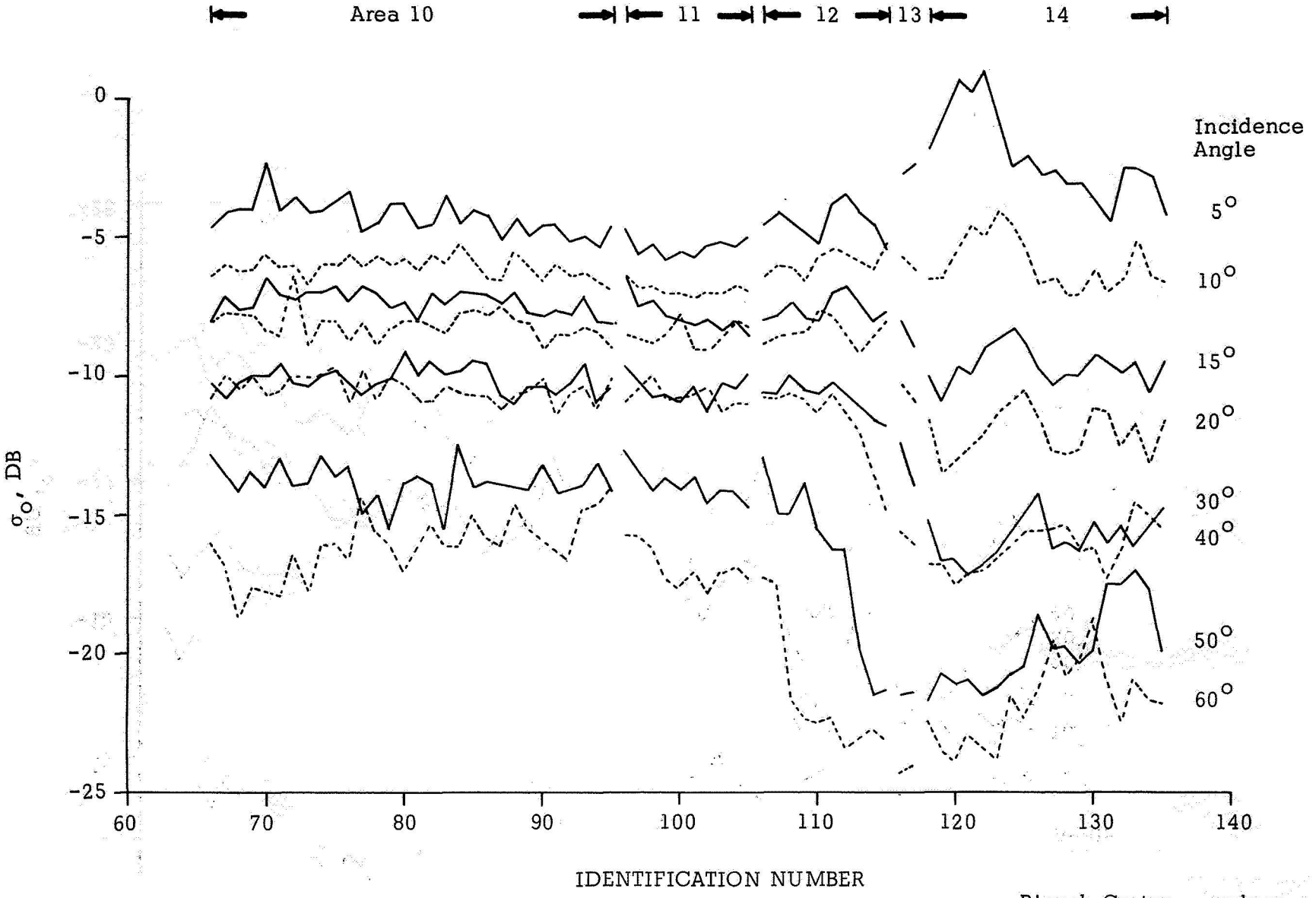

Pisgah Crater σ_o values

Forebeam, M21-F5-L1-R3

Figure 4.

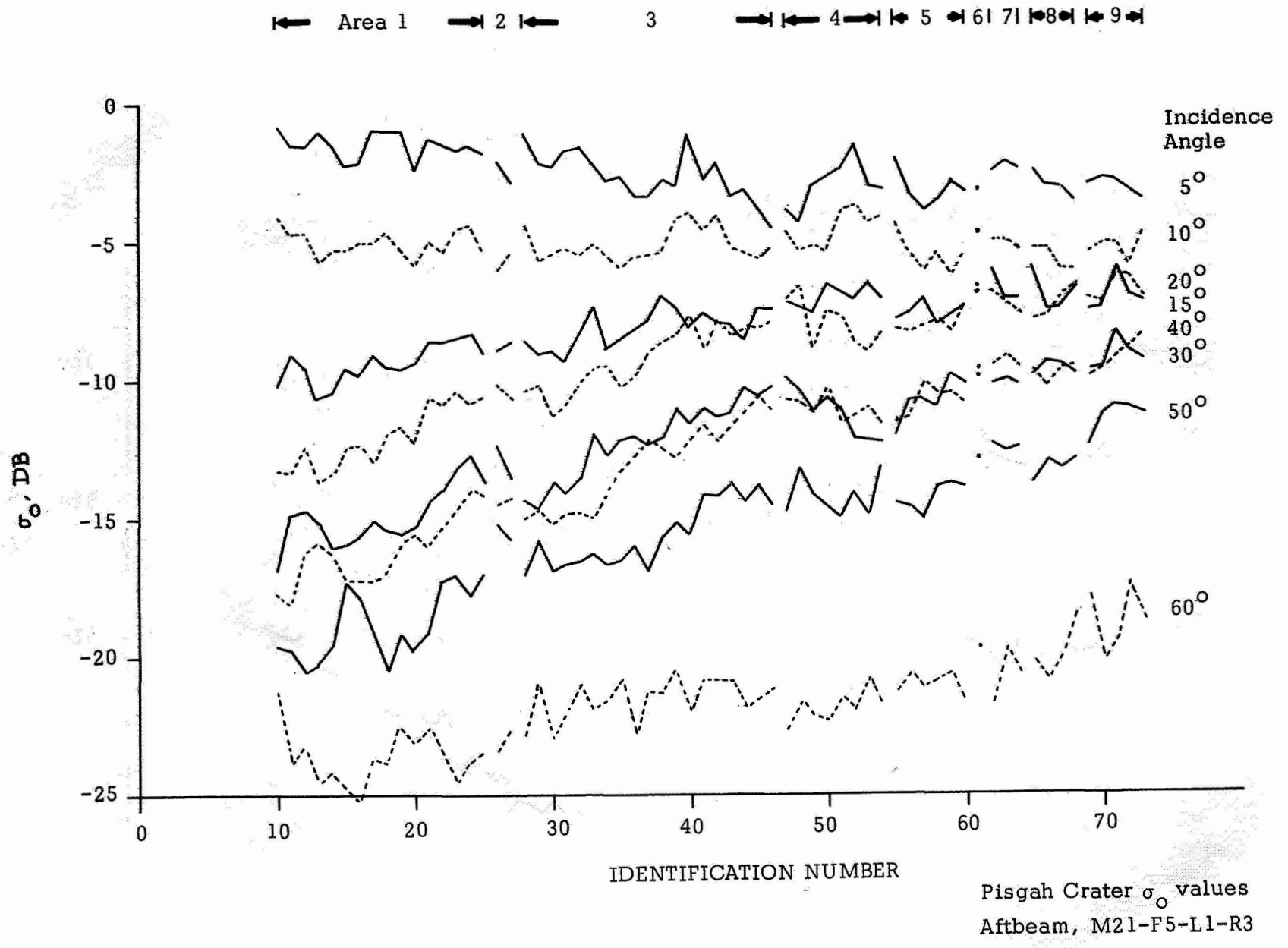
Area 1
2
3
4
5
6
7
8
9
Incidence Angle
5°
10°
20°
15°
40°
30°
50°
60°
0
-5
-10
-15
-20
-25
σo, DB
0
10
20
30
40
50
60
70
IDENTIFICATION NUMBER
Pisgah Crater σo values
Aftbeam, M21-F5-L1-R3

Figure 5.

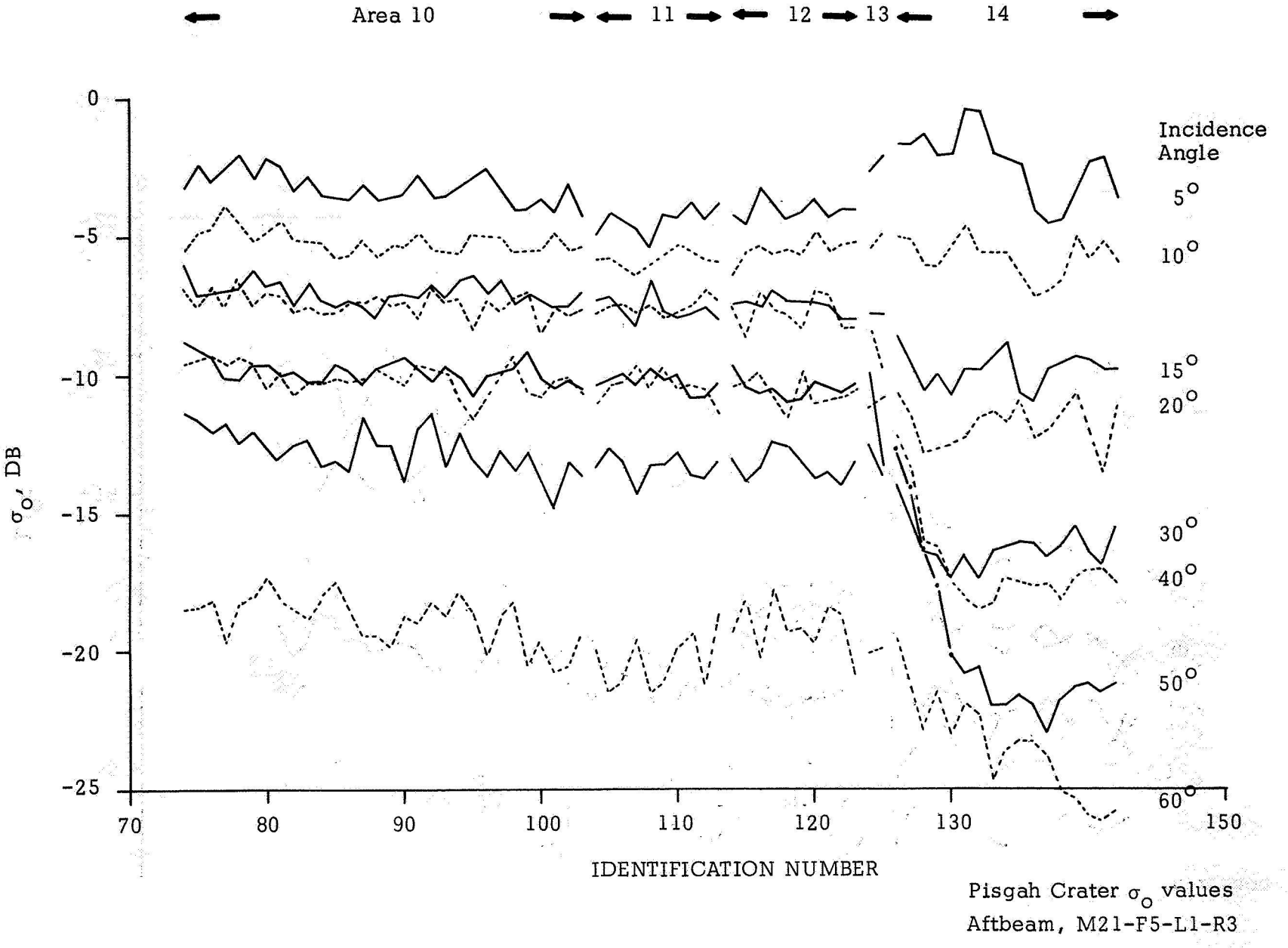
Area 10
11
12
13
14
0
-5
-10
-15
-20
-25
σ_o, DB
70
80
90
100
110
120
130
150
IDENTIFICATION NUMBER
Incidence Angle
5°
10°
15°
20°
30°
40°
50°
60°
Pisgah Crater σ_o values
Aftbeam, M21-F5-L1-R3

Figure 6.

Scatterometer Mission 21, Flight 5, Line 1, Run 3 -- Flight Information

Altitude -- Between 4000 and 4200 feet
Ground Speed -- 160 knots
Drift -- 1.0 degree left (average)
Resolution Cell Length -- 202 feet

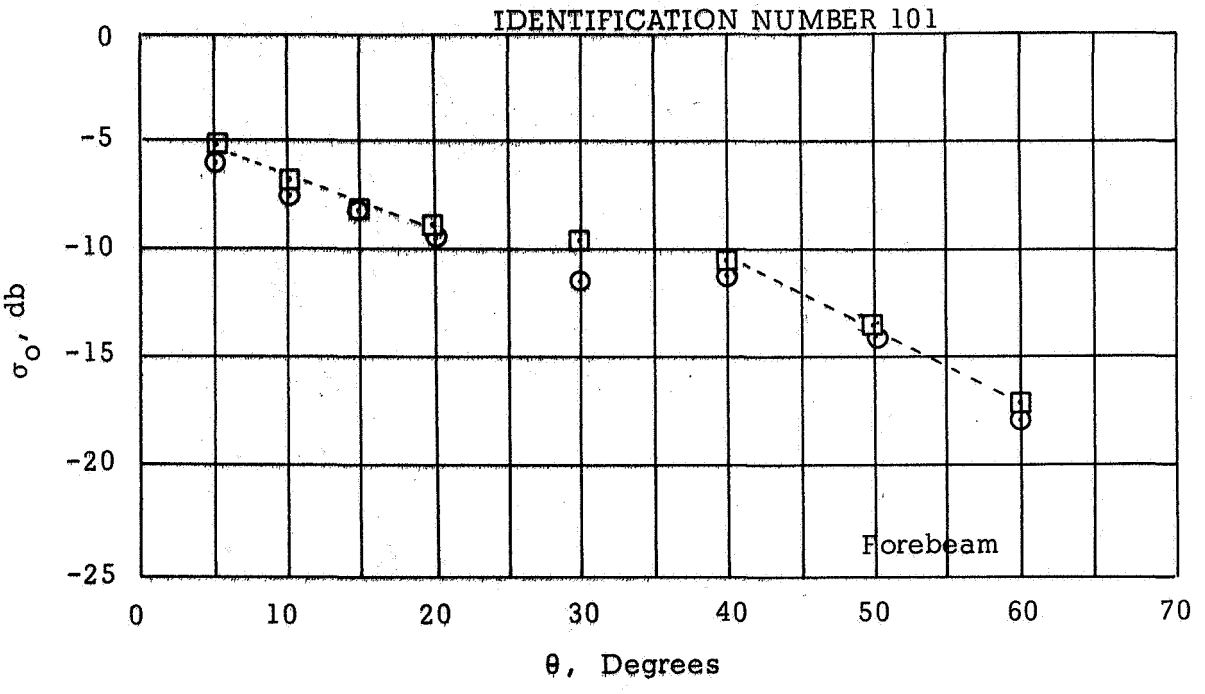

Legend:

⊡ First of 2-resolution-cell pair

⊙ Second of 2-resolution-cell pair

Example of σ_o vs θ curve

Figure 7.

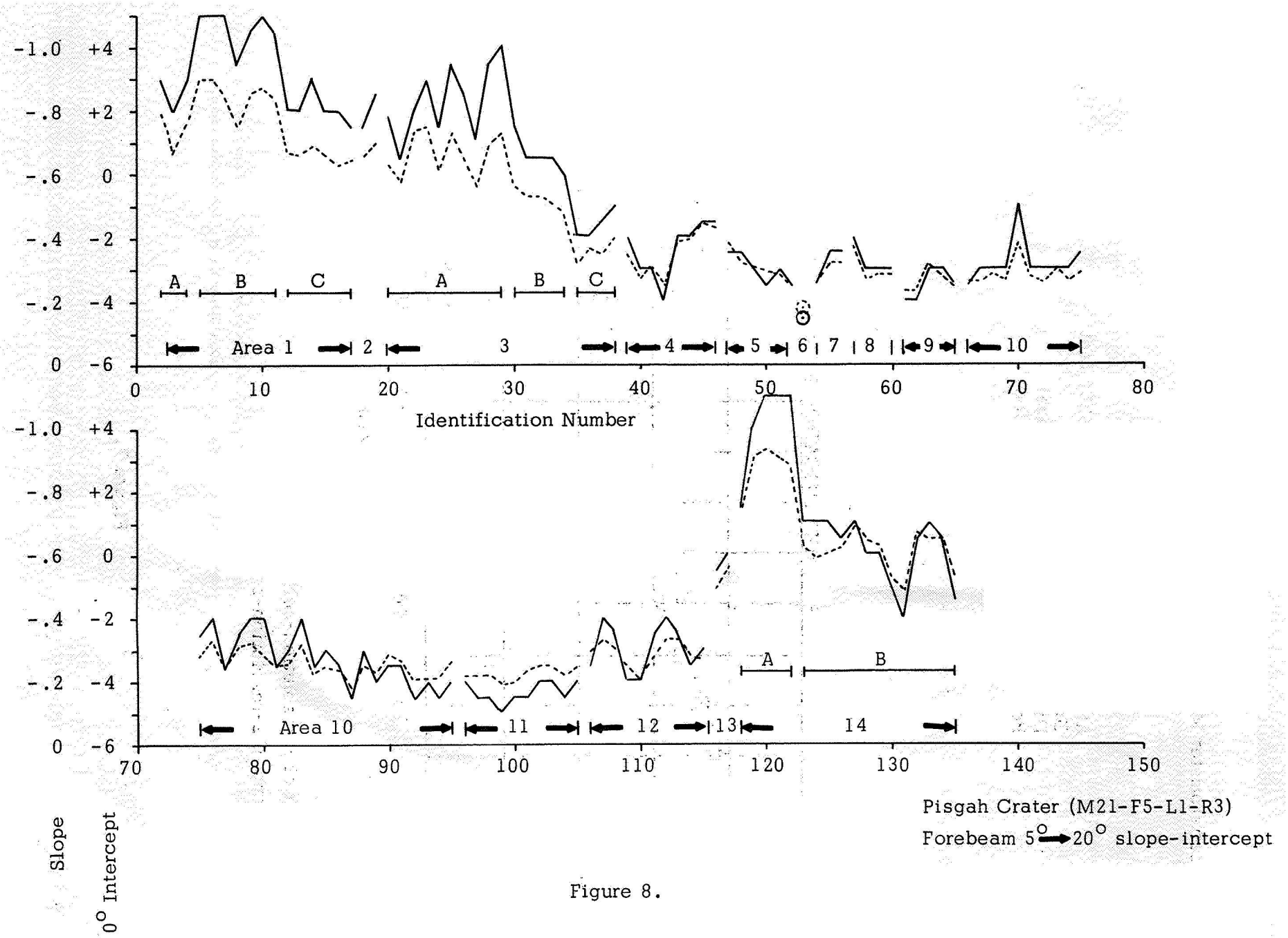
-1.0
-.8
-.6
-.4
-.2
0
+4
+2
0
-2
-4
-6
A
B
C
Area 1
2
3
4
5
6
7
8
9
10
0
10
20
30
40
50
60
70
80
Identification Number
Area 10
11
12
13
14
90
100
110
120
130
140
150
Slope
0° Intercept
Pisgah Crater (M21-F5-L1-R3)
Forebeam 5°→20° slope-intercept

Figure 8.

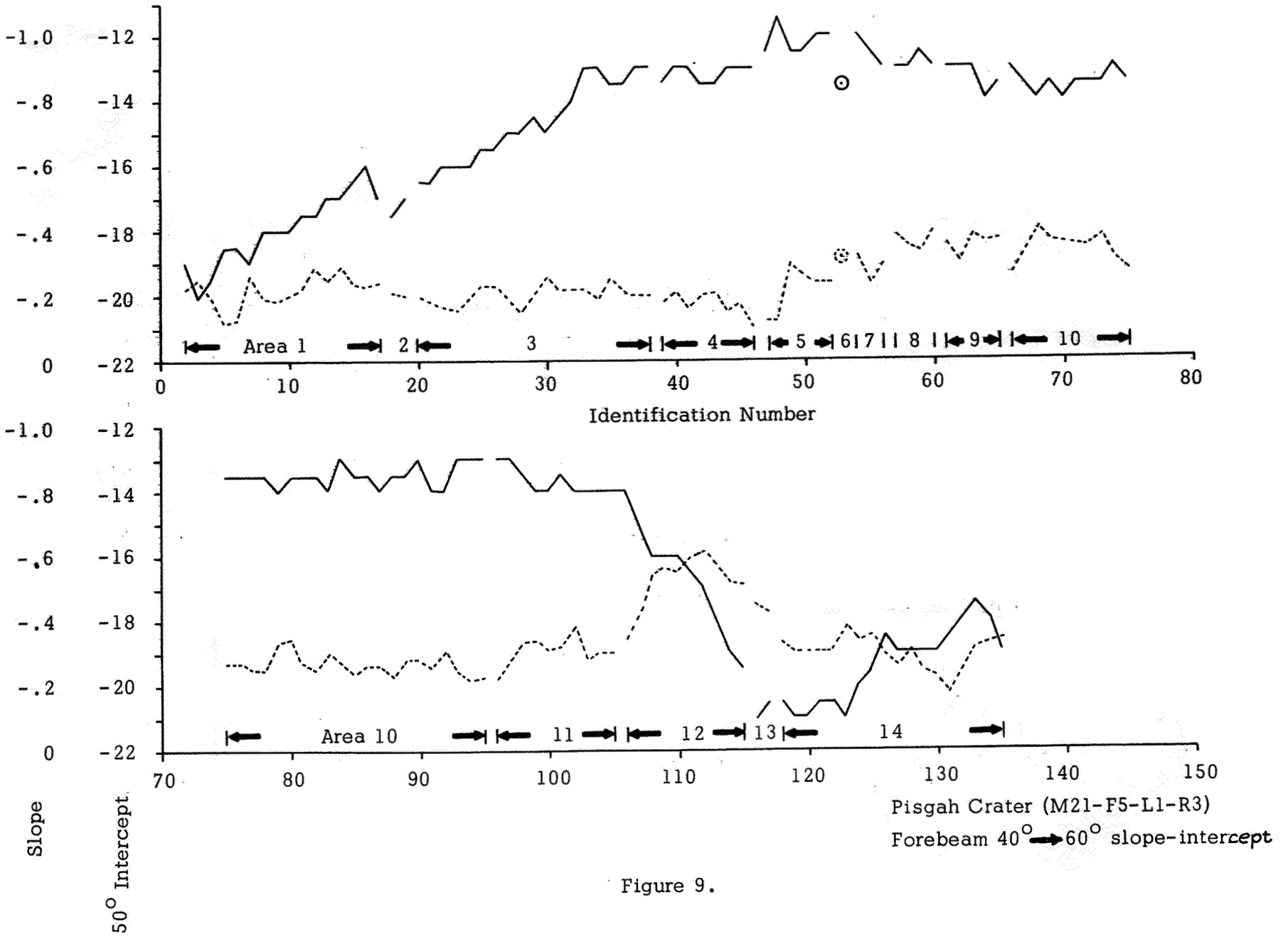
-1.0
-.8
-.6
-.4
-.2
0
-12
-14
-16
-18
-20
-22
Area 1
2
3
4
5
6
7
8
9
10
0
10
20
30
40
50
60
70
80
Identification Number
Area 10
11
12
13
14
70
80
90
100
110
120
130
140
150
Pisgah Crater (M21-F5-L1-R3)
Forebeam 40° → 60° slope-intercept
Slope
50° Intercept

Figure 9.

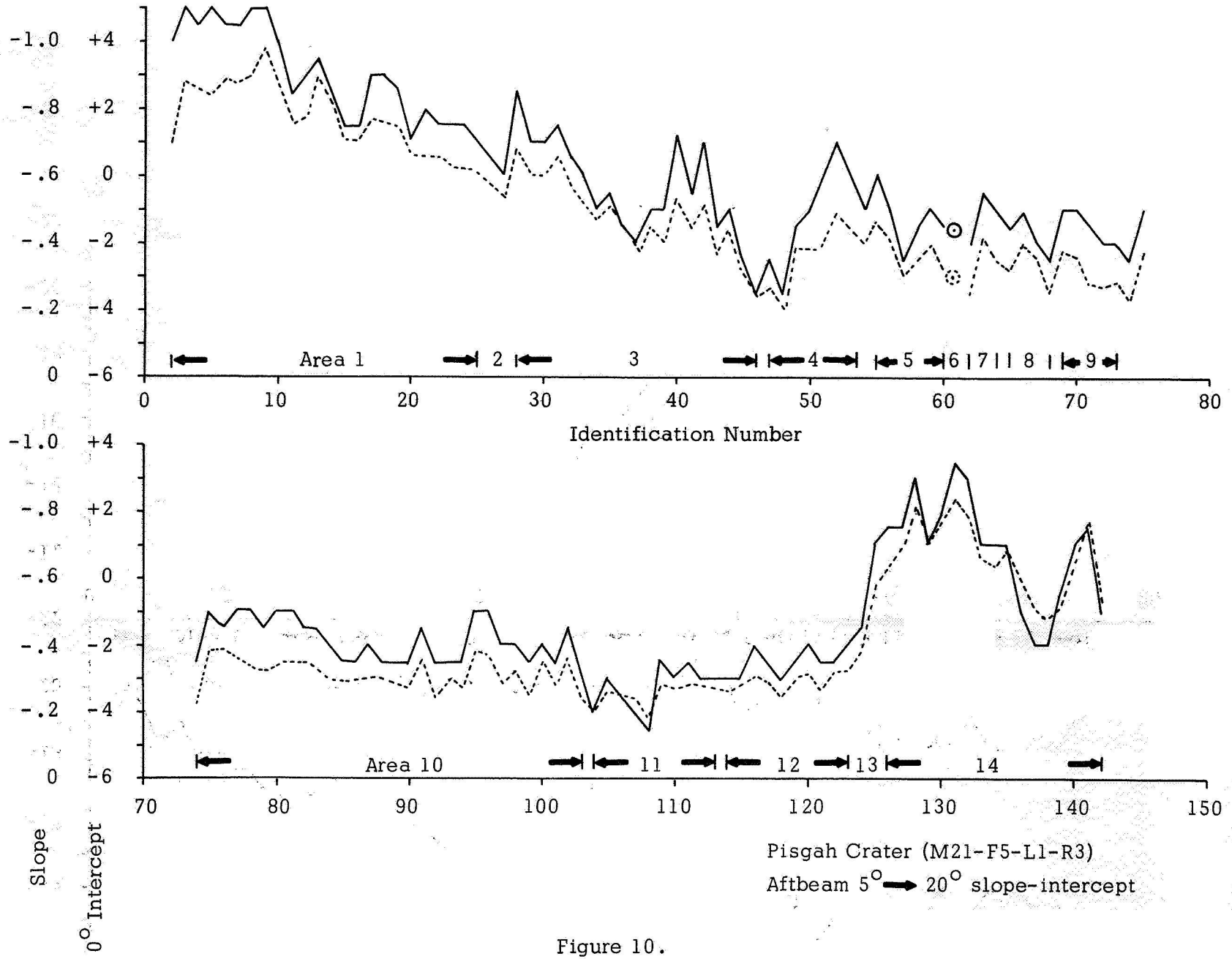
-1.0
-.8
-.6
-.4
-.2
0
+4
+2
0
-2
-4
-6
Area 1
2
3
4
5
6
7
8
9
0
10
20
30
40
50
60
70
80
Identification Number
Area 10
11
12
13
14
70
80
90
100
110
120
130
140
150
Slope
0° Intercept
Pisgah Crater (M21-F5-L1-R3)
Aftbeam 5° → 20° slope-intercept

Figure 10.

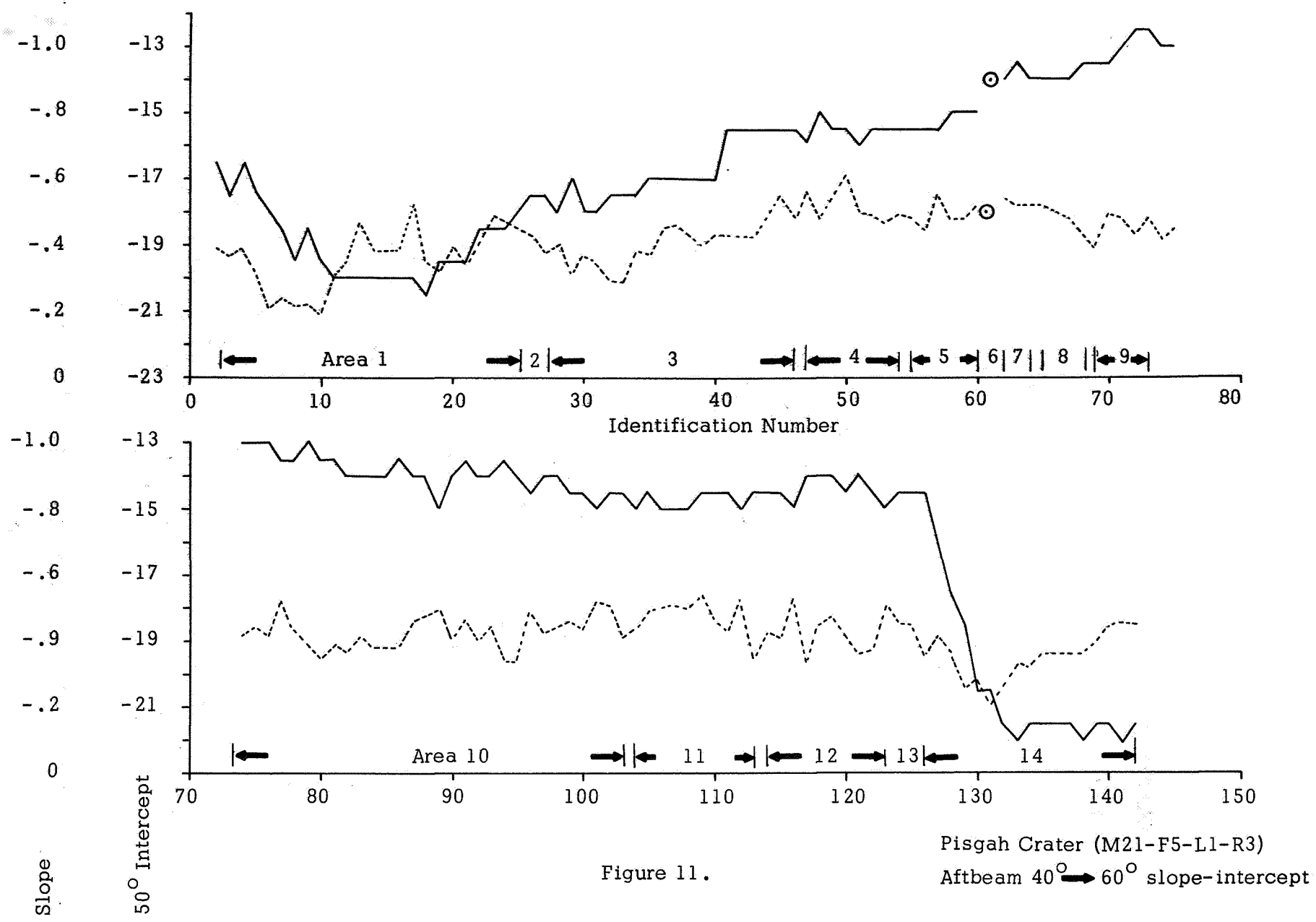

Figure 11.

Pisgah Crater (M21-F5-L1-R3)
Aftbeam 40° → 60° slope-intercept

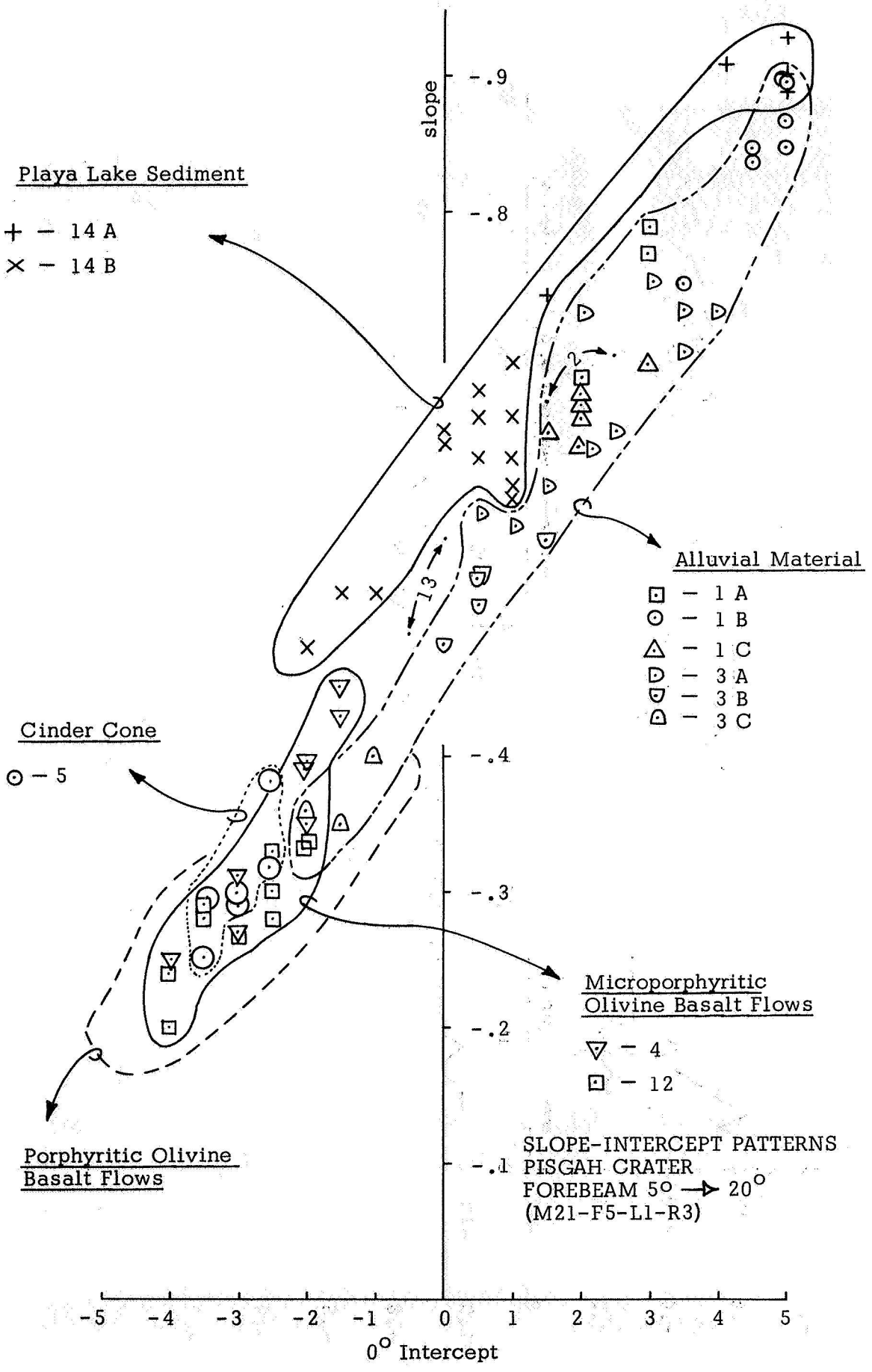
slope
-.9
-.8
-.4
-.3
-.2
-.1
Playa Lake Sediment
+ — 14 A
× — 14 B
Alluvial Material
□ — 1 A
⊙ — 1 B
△ — 1 C
▷ — 3 A
▽ — 3 B
⌓ — 3 C
Cinder Cone
⊙ — 5
Microporphyritic
Olivine Basalt Flows
▽ — 4
□ — 12
Porphyritic Olivine
Basalt Flows
SLOPE-INTERCEPT PATTERNS
PISGAH CRATER
FOREBEAM 5° → 20°
(M21-F5-L1-R3)
-5 -4 -3 -2 -1 0 1 2 3 4 5
0° Intercept

Figure 12.

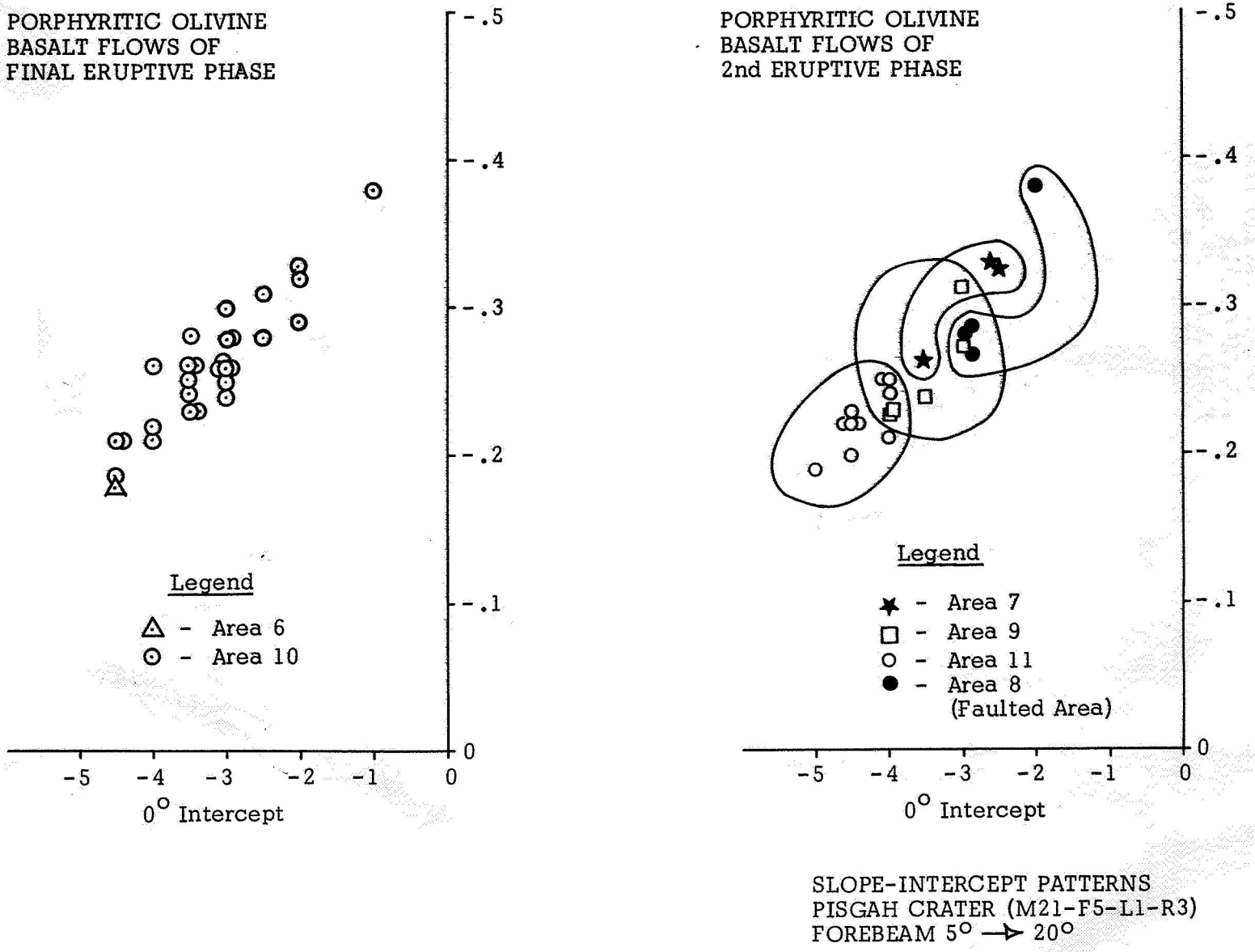
PORPHYRITIC OLIVINE
BASALT FLOWS OF
FINAL ERUPTIVE PHASE
Legend
△ - Area 6
⊙ - Area 10
0° Intercept
PORPHYRITIC OLIVINE
BASALT FLOWS OF
2nd ERUPTIVE PHASE
Legend
★ - Area 7
□ - Area 9
○ - Area 11
● - Area 8
(Faulted Area)
0° Intercept
SLOPE-INTERCEPT PATTERNS
PISGAH CRATER (M21-F5-L1-R3)
FOREBEAM 5° → 20°

Figure 13.

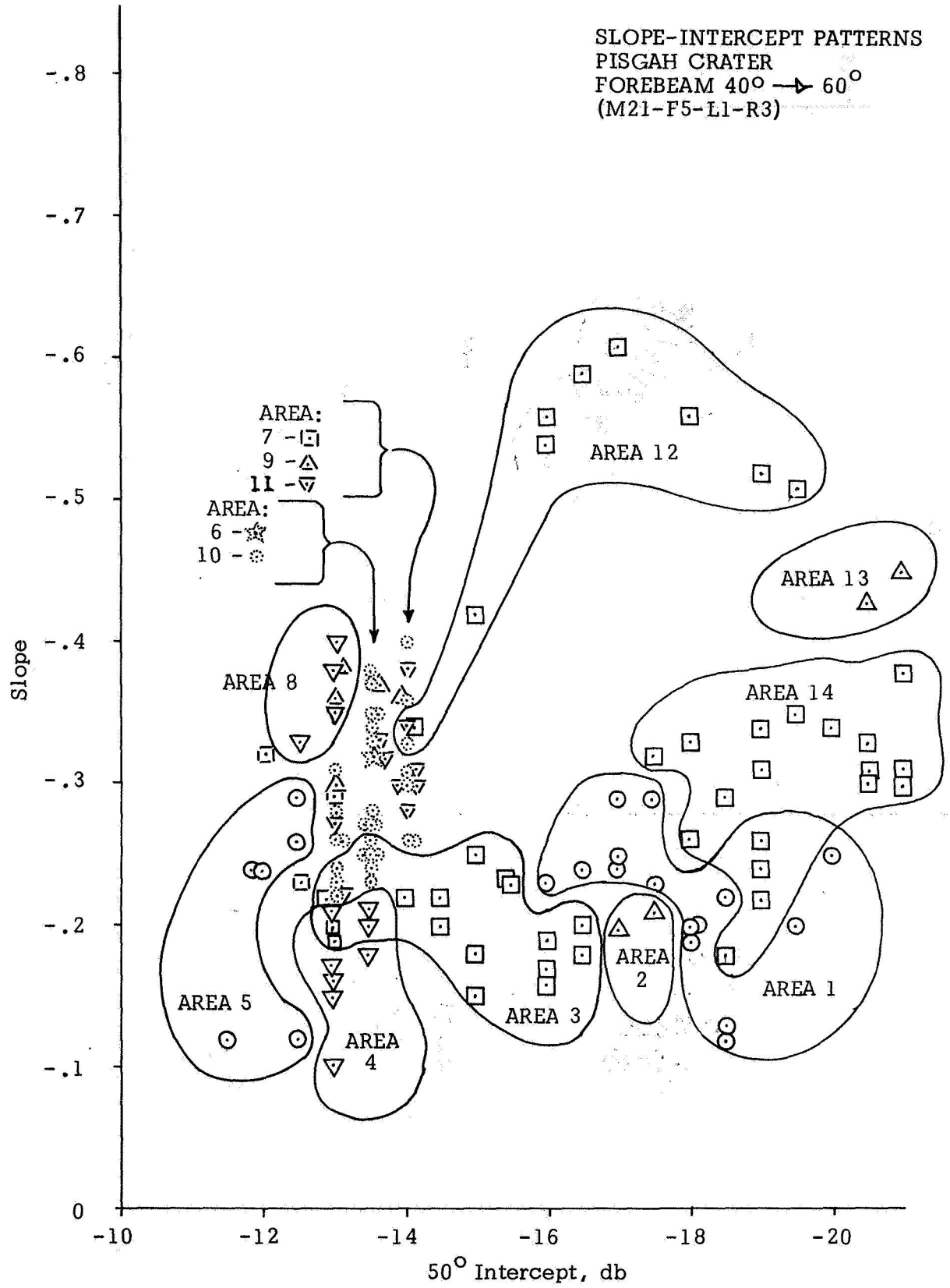
SLOPE-INTERCEPT PATTERNS
PISGAH CRATER
FOREBEAM 40° → 60°
(M21-F5-L1-R3)
AREA:
7 -
9 -
11 -
AREA:
6 -
10 -
AREA 12
AREA 13
AREA 14
AREA 8
AREA 5
AREA 4
AREA 3
AREA 2
AREA 1
Slope
-.8
-.7
-.6
-.5
-.4
-.3
-.2
-.1
0
-10
-12
-14
-16
-18
-20
50° Intercept, db

Figure 14.

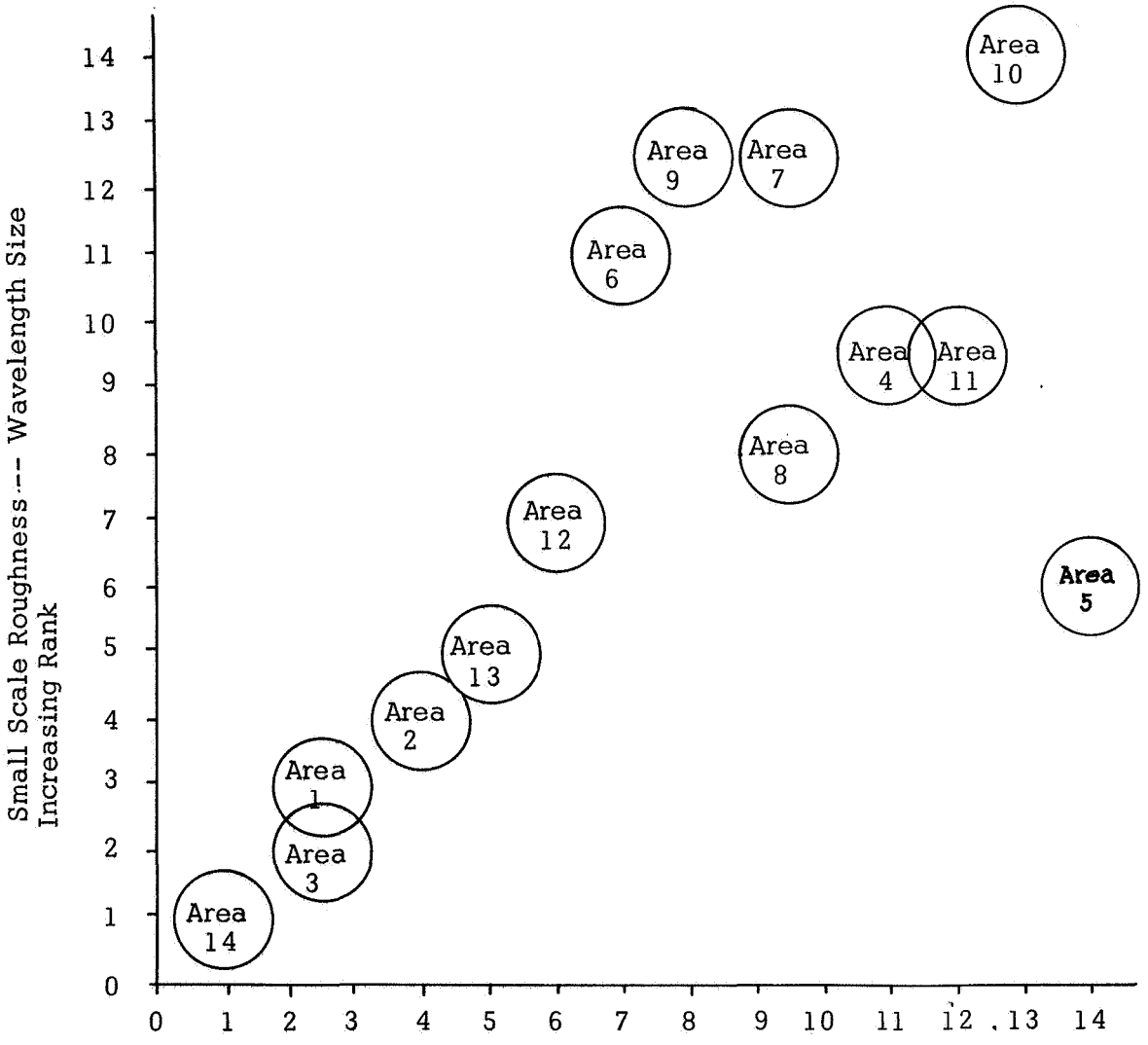

ROUGHNESS RANK
OF 14 GEOLOGIC AREAS
ON PISGAH CRATER
FLIGHT LINE

Figure 15.

UNCLASSIFIED
Security Classification

DOCUMENT CONTROL DATA - R & D

(Security classification of title, body of abstract and indexing annotation must be entered when the overall report is classified)

1. ORIGINATING ACTIVITY *(Corporate author)*
Center for Research in Engineering Science (CRES)
Remote Sensing Laboratory
University of Kansas, Lawrence, Kansas 66044

2a. REPORT SECURITY CLASSIFICATION
UNCLASSIFIED

2b. GROUP

3. REPORT TITLE
Analysis of Scatterometry Data from Pisgah Crater

4. DESCRIPTIVE NOTES *(Type of report and inclusive dates)*

5. AUTHOR(S) *(First name, middle initial, last name)*
Jerry R. Lundien

6. REPORT DATE	7a. TOTAL NO. OF PAGES	7b. NO. OF REFS
August 1967	36	4

8a. CONTRACT OR GRANT NO.	9a. ORIGINATOR'S REPORT NUMBER(S)
NASA Contract NSR 17-004-003 and b. PROJECT NO. NAS 9-7175	CRES Technical Report 118-2
c.	9b. OTHER REPORT NO(S) *(Any other numbers that may be assigned this report)*
d.	

10. DISTRIBUTION STATEMENT

11. SUPPLEMENTARY NOTES	12. SPONSORING MILITARY ACTIVITY

13. ABSTRACT

DD FORM 1 NOV 65 1473

UNCLASSIFIED
Security Classification

KEY WORDS	LINK A		LINK B		LINK C	
	ROLE	WT	ROLE	WT	ROLE	WT
1. Radar						
2. Scatterometer						
3. Fan beam radar						
4. Scattering vs. incidence angle						
5. Doppler						
6. Methods of data analysis						
7. Earth Science applications						
8. Geology						
9. Lava						
10. Sediments						